RSC Advances

PAPER

View Article Online
View Journal | View Issue

Cite this: *RSC Adv.*, 2017, **7**, 8936

Structural stability and thermoelectric property optimization of Ca_2Si

Rui Xiong,[a] Baisheng Sa,*[ab] Naihua Miao,[b] Yan-Ling Li,[c] Jian Zhou,[b] Yuanchun Pan,[b] Cuilian Wen,*[a] Bo Wu[a] and Zhimei Sun*[b]

Received 13th December 2016
Accepted 24th January 2017

DOI: 10.1039/c6ra28125g

rsc.li/rsc-advances

By using an *ab initio* evolutionary algorithm structure search, low enthalpy criterion as well as stability analysis, we have found that cubic $Fm\bar{3}m$ Ca_2Si can be achieved under a negative external pressure, and the cubic phase is dynamically and mechanically stable at ambient conditions and high pressure. From first-principle hybrid functional calculations, we have unraveled the direct bandgap nature and bandgap variation of cubic $Fm\bar{3}m$ Ca_2Si with respective to pressure. Moreover, by combining with Boltzmann transport theory and the phonon Boltzmann transport equation, we have predicted that the figure of merit ZT for the cubic $Fm\bar{3}m$ Ca_2Si reaches the maximum value of 0.52 by p-type doping. Our results provide an interesting insight and feasible guidelines for the potential applications of cubic $Fm\bar{3}m$ Ca_2Si and related alkaline-earth metals silicides as the thermoelectric materials for heat-electricity energy convertors.

1. Introduction

Thermoelectric materials have received global attention because of their potential application in heat-electricity energy conversion, power generation and cooling thermoelectric devices.[1,2] Many specialized applications have been realized in the thermoelectric devices due to high reliability, good scalability and simple device structure. The efficiency of thermoelectric devices can be determined by a dimensionless figure of merit $ZT = TS^2\sigma/\kappa$, where T, S, σ and κ ($\kappa = \kappa_l + \kappa_e$) are the absolute temperature, the Seebeck coefficient, electrical conductivity and thermal conductivity (as the sum of the lattice and electronic contributions), respectively. The product of $S^2\sigma$ is the thermoelectric power factor (PF) which should be maximized and the thermal conductivity κ should be minimized to achieve the expected high thermoelectric performance. The typical ways to optimize ZT are alloying,[3,4] pressure & strain engineering,[5,6] nanostructuring[7] and low dimensioning.[8,9] Besides, the investigations of novel thermoelectric materials with intrinsic high ZT value are still anticipated.[10]

Since 1950, the Bi_2Te_3-based chalcogenides have been developed and proposed as the best materials for room-temperature thermoelectric applications.[11–13] The α-MgAgSb-based materials with the high $ZT \sim 1$ near room-temperature has been recently reported to be the candidates of the next generation thermoelectric energy production materials.[14–16] Unfortunately, the high-cost and scarcity of Te and Ag elements hinder the commercial applications of these thermoelectric materials in large scale. Recently, the semiconducting alkaline-earth metals (AEMs) silicides have gained great attention for their potential applications in the thermoelectric power generator utilizing waste heat sources.[17,18] Ca_2Si is one of the environmental friendly and inexpensive AEMs, which can be synthesized by the heat treatment from the Mg_2Si powders under Ca vapor.[19,20] It is interesting to see that the Seebeck coefficient of $\sim$300 $\mu V\ K^{-1}$ with p-type conduction nature of Ca_2Si was experimentally measured.[21] However, in ambient condition Ca_2Si is stabilized in the orthorhombic phase with a space group of *Pnma*.[22] Considering the fact that the high symmetry cubic phase present larger number of equivalent degenerated valleys of the electronic structure than the low symmetry orthorhombic phase, better performance of the thermoelectric properties of cubic Ca_2Si is anticipated. And the low symmetry of the orthorhombic phase leads to the anisotropic mechanical and optical properties,[23,24] which is not desired associated with the Cannikin law. From the self-consistent scalar-relativistic full potential linearized augmented plane wave (FPLAPW) calculation, cubic Ca_2Si shows smaller bandgap value then the orthorhombic phase.[25,26] The authors also assumed that suitable cubic substrate like diamond can help the growth of the cubic Ca_2Si.[25] It is worth noting that as the silicon source and crystal template, Mg_2Si is crystallized in the cubic phase with the space group of $Fm\bar{3}m$, which is isotropic.[27,28] But till now, the cubic Ca_2Si is not experimentally observed. Hence theoretically, a more complete picture is required to elucidate the existence condition of cubic Ca_2Si.

[a]*College of Materials Science and Engineering, Fuzhou University, and Key Laboratory of Eco-materials Advanced Technology (Fuzhou University), Fujian Province University, Fuzhou 350100, P. R. China. E-mail: bssa@fzu.edu.cn; clwen@fzu.edu.cn*

[b]*School of Materials Science and Engineering, and Center for Integrated Computational Materials Engineering, International Research Institute for Multidisciplinary Science, Beihang University, 100191 Beijing, P. R. China. E-mail: zmsun@buaa.edu.cn*

[c]*School of Physics and Electronic Engineering, Jiangsu Normal University, 221116, Xuzhou, People's Republic of China*

Applying external pressure is an effective way to stabilize the metastable or unstable phases of materials.[29–31] In this work, by means of the *ab initio* evolutionary algorithm calculations, we have revealed the stable conditions for the Ca_2Si isomers under a wide (including positive and negative) pressure range. We found that the cubic phase of Ca_2Si is a metastable phase under negative pressure and can be stabilized to the ambient condition, such negative-pressure condition could be probably achieved by increasing the synthetic temperature. Based on further density functional theory calculations combined with Boltzmann transport theory, we have systematically analyzed the electronic structure, lattice dynamical properties and the thermoelectric properties for cubic Ca_2Si.

2. Computational details

We studied Ca_2Si based on density functional theory (DFT) using the Vienna *ab initio* simulation package[32] (VASP) in conjunction with projector augmented wave (PAW) pseudopotentials within the generalized gradient approximations[33] (GGA) of Perdew–Burke–Ernzerhof[34] (PBE). Structure searches for the Ca_2Si isomers under positive and negative pressures were carried out through the *ab initio* evolutionary algorithm (EA) using the USPEX code.[35,36] The valence electron configuration for Ca and Si were $3s^2 3p^6 4s^2$ and $3s^2 3p^2$ respectively. The cutoff energy for the plane-wave was set to 600 eV. The first Brillouin zone (1BZ) was sampled with a grid of $11 \times 11 \times 11$ for the cubic phase and equivalent dense for the other phases in the structure optimization and energy calculation processes. The YPHON[37] code was applied to obtain the phonon frequencies through the density functional perturbation theory (DFPT) methods[38] with $2 \times 2 \times 2$ supercells and $3 \times 3 \times 3$ *K*-points sampling. The thermodynamic properties were gained by using the quasi-harmonic approximation (QHA) method.[39] The relaxation convergence for both ions and electrons were 1×10^{-6} eV. The crystal structures were visualized using the VESTA[40] tool. It is well known that PBE calculations normally underestimate the electronic band gap, and the hybrid function with the mixing of the Hartree–Fock and DFT exchange terms is thought to be a practical solution to solve the band gap problem.[41,42] Herein, we introduced the Heyd–Scuseria–Ernzerhof (HSE06) hybrid functional[43] to precisely evaluate the bandgap of Ca_2Si. The thermoelectric properties were computed from the semi-classical Boltzmann transport theory within the constant relaxation time approximation ($\tau = 10^{-15}$ s, which is a normal magnitude for relaxation time in semiconductors[44]) and a rigid band approach using the BoltzTraP code.[45] For the prediction of the thermoelectric properties, denser *k*-point meshes (twice as large as for the geometry optimization) were adopted for Brillouin zone integration to ensure the convergence and accuracy of eigenvalues. The second harmonic force constants from the Phonopy[46] package and the third order anharmonic interatomic force constants created by the ShengBTE[47] code with $4 \times 4 \times 4$ supercells and gamma *K*-point sampling were introduced to evaluate the lattice thermal conductivity.

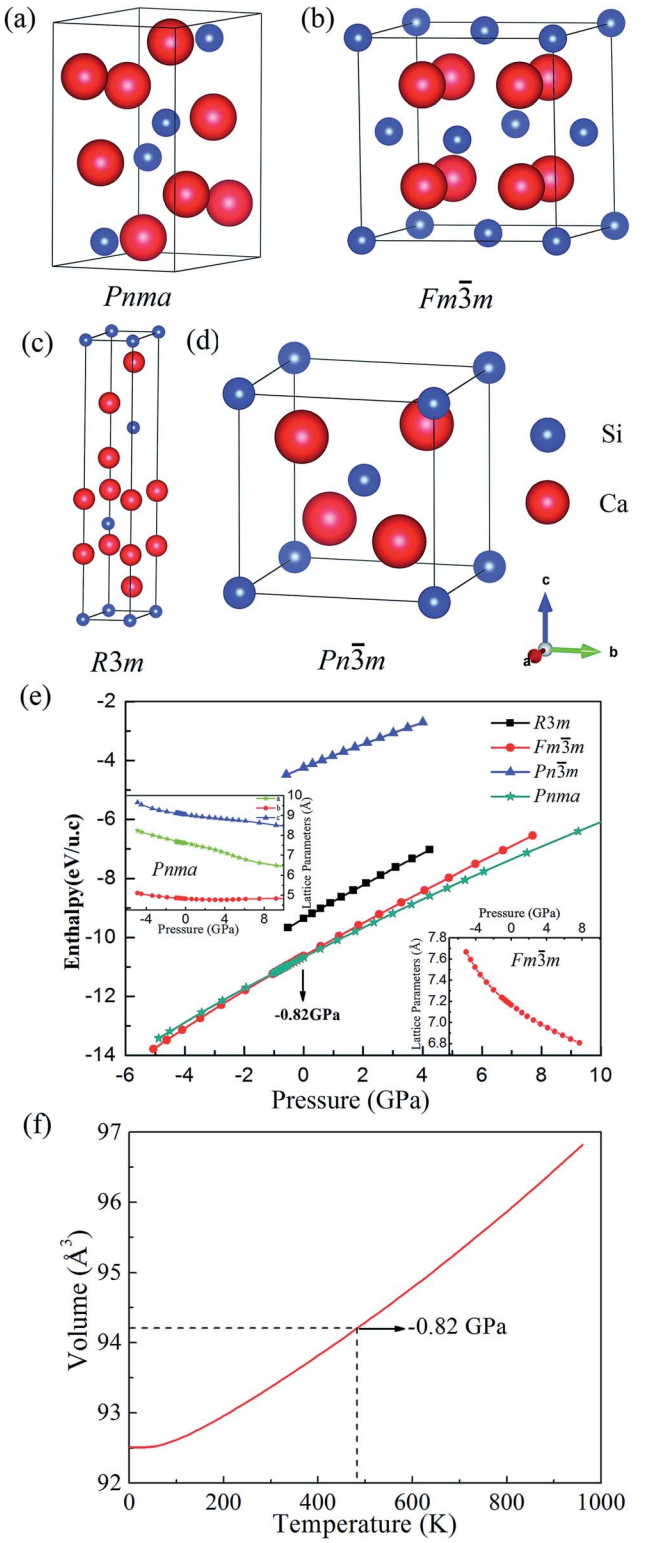

Fig. 1 The crystal structures of (a) *Pnma*, (b) *Fm*$\bar{3}$*m*, (c) *R*3*m* and (d) *Pn*$\bar{3}$*m* Ca_2Si, respectively. (e) The enthalpy as a function of pressure for the predicted phases of Ca_2Si, the insert figures show the pressure dependence of the lattice constants of *Pnma* and *Fm*$\bar{3}$*m* Ca_2Si and (f) the volume as a function of temperature for *Fm*$\bar{3}$*m* Ca_2Si.

3. Results and discussions

We have found four possible structures for Ca_2Si, which belong to the space groups of *Pnma* (Fig. 1(a)), $Fm\bar{3}m$ (Fig. 1(b)), $R3m$ (Fig. 1(c)) and $Pn\bar{3}m$ (Fig. 1(d)), respectively. The equilibrium lattice parameters and atomic Wyckoff positions for the predicted phases at the ambient condition are listed in Tables 1 and 2. Herein the *Pnma* phase refers to the orthorhombic phase which has been experimentally synthesized. At the ambient condition, our GGA-PBE relaxed lattice parameters for orthorhombic *Pnma* Ca_2Si are $a = 7.605$, $b = 4.821$, $c = 9.038$, agree well with the experimental results within less than 1% mismatch.[48] The $Fm\bar{3}m$ and $Pn\bar{3}m$ are two cubic phases. It is obvious that the $Fm\bar{3}m$ phase is more close-packing than the $Pn\bar{3}m$ phase, indicating that the $Fm\bar{3}m$ phase is more stable. In fact, the $Fm\bar{3}m$ phase shows the same crystal structure as stable Mg_2Si. Our calculated lattice constant a is 7.165 Å for the cubic $Fm\bar{3}m$ Ca_2Si at the ambient condition, which is in good agreement with the previous theoretical prediction.[25] Fig. 1(e) illustrates the enthalpies *vs.* pressure curves of Ca_2Si in difference space groups. As we can see from the figure that *Pnma* and $Fm\bar{3}m$ phases hold very close enthalpy, which locate at obviously lower level than the $R3m$ and $Pn\bar{3}m$ cases. Hence in the full pressure range, the *Pnma* and $Fm\bar{3}m$ phases are favorable. Moreover, one can see that the *Pnma* phase is the most stable structure at the ambient condition and the full positive pressure range. The $Fm\bar{3}m$ phase become the most stable one only under a negative external pressure of −0.82 GPa. To achieve such negative pressure condition, we can experimentally enhance the synthesis temperature. As seen in Fig. 1(f), the equilibrium volume of cubic $Fm\bar{3}m$ Ca_2Si gradually increases with the increase of the temperature. The volume of cubic $Fm\bar{3}m$ Ca_2Si at −0.82 GPa (the transition pressure) is 94.22 $Å^3$, corresponding to the environmental temperature around 480 K. Hence we assume that the synthetic temperature higher than 480 K is necessary to achieve the cubic $Fm\bar{3}m$ Ca_2Si. The insert figures in Fig. 1(e) show the pressure dependence of the lattice constants

Table 1 The calculated cohesive energy and equilibrium lattice parameters for the predicted phases of Ca_2Si at the ambient condition

Phase	E_0 (eV per u.c.)	a_0 (Å)	b_0 (Å)	c_0 (Å)	α (°)	β (°)	γ (°)
Pnma	−10.667	7.605	4.821	9.038	90	90	90
Pnma[25]	−10.773	7.618	4.793	9.001	90	90	90
Pnma[47]	Expt.	7.691	4.816	9.035	90	90	90
$Fm\bar{3}m$	−10.623	7.165	7.165	7.165	90	90	90
$Fm\bar{3}m$[25]	−10.740	7.148	7.148	7.148	90	90	90
$R3m$	−9.352	3.819	3.819	22.748	90	90	120
$Pn\bar{3}m$	−8.473	6.435	6.435	6.435	90	90	90

Table 2 The atomic Wyckoff positions for the predicted phases of Ca_2Si at the ambient condition

Phase	Atom	Site	x	y	z
Pnma	Ca1	4c	0.3459	0.2500	0.0742
	Ca2	4c	0.9802	0.2500	0.8221
	Si1	4a	0.7476	0.2500	0.1052
$Fm\bar{3}m$	Ca1	8c	0.2500	0.2500	0.2500
	Ca2	8c	0.7500	0.7500	0.7500
	Si1	4a	0.0000	0.0000	0.0000
$R3m$	Ca1	3a	0.0000	0.0000	0.2500
	Ca2	3a	0.0000	0.0000	0.7500
	Si1	3a	0.0000	0.0000	0.0000
$Pn\bar{3}m$	Ca1	4b	0.7500	0.7500	0.2500
	Ca2	4b	0.2500	0.2500	0.2500
	Si1	2a	0.5000	0.5000	0.5000

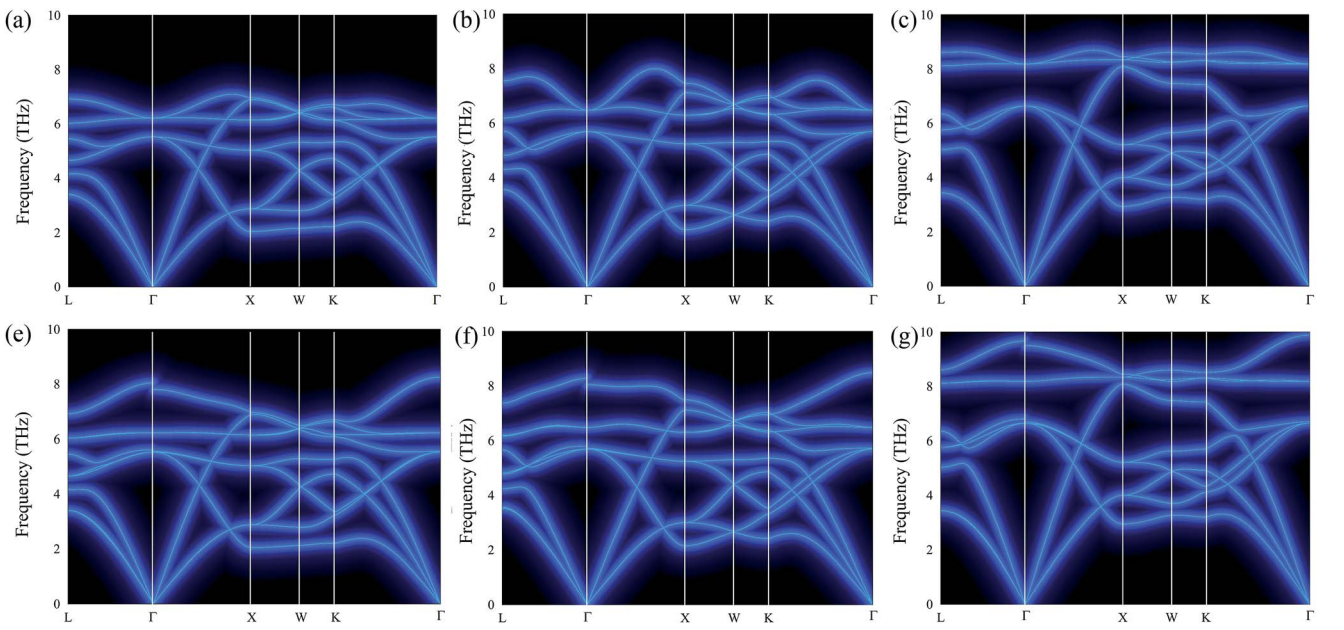

Fig. 2 The calculated phonon dispersion curves of cubic $Fm\bar{3}m$ Ca_2Si (a–c) without and (e–g) with LO–TO splitting, where (a) and (e) at −0.82 GPa external pressure, (b) and (f) at the ambient condition, (c) and (g) at 7.8 GPa external pressure.

of *Pnma* and $Fm\bar{3}m$ Ca_2Si, we found that the lattice constants of both the phases decrease gradually with the increase of the external pressure. Considering the fact that the enthalpy difference between the *Pnma* and $Fm\bar{3}m$ phases is as small as 44 meV per u.c. (unit cell), it is natural to expect that the cubic $Fm\bar{3}m$ phase might be stabilized at the ambient condition as well as under finite positive external pressure.

To investigate the stability of cubic $Fm\bar{3}m$ Ca_2Si under different pressures, we calculated the phonon dispersion curves both without and with LO–TO splitting in the first Brillouin zone (1BZ), which are illustrated in Fig. 2. As we can see, no negative or imaginary frequency was found in cubic $Fm\bar{3}m$ Ca_2Si for all the cases. The results suggest that cubic $Fm\bar{3}m$ Ca_2Si shows very good lattice dynamical stability at the pressure range we have studied. Hence the $Fm\bar{3}m$ structure is a metastable phase of Ca_2Si under pressure higher than −0.82 GPa. With the increase of pressure, the Ca–Si bonds were compressed, resulting in the increase of the maximum dispersion frequencies of the optical modes. Without LO–TO splitting, the calculated maximum frequencies of the twofold degenerated optical modes at the Γ point are 6.2 THz, 6.5 THz and 8.1 THz under −0.82 GPa negative pressure, at the ambient condition and under a positive pressure of 7.8 GPa, respectively. The LO–TO splitting is accounted by collecting the Born effective charge tensor and dielectric constant tensor. Under the influence of LO–TO splitting, we found that the twofold degenerated optical modes at the Γ point split into a higher frequency discontinue LO branch and a lower frequency TO branch. The TO branch holds the frequency of the optical branches without LO–TO splitting. The discontinuity of the LO branch is due to the difference in the magnitude of LO–TO splitting along the L–Γ and Γ–X directions.[49] It is well known that the soft mode of the acoustic branch is the critical feature of a material with low lattice thermal conductivity, which is expected to achieve high ZT.[50] We have found that cubic $Fm\bar{3}m$ Ca_2Si represents very similar soft mode characteristics to cubic $Fm\bar{3}m$ Mg_2Si.[51] It is worth noting that the low frequency optical branches overlap with the acoustic branches along the X–W–K path are softer than Mg_2Si. Hence lower lattice thermal conductivity in cubic $Fm\bar{3}m$ Ca_2Si is anticipated. On the other hand, similar to Mg_2Si, the increase of external pressure leads to the frequency enhancement of the soft modes, which is not expected for thermoelectric applications.

In additions, to further confirm the stability of cubic $Fm\bar{3}m$ Ca_2Si, we predicted the mechanical stability *via* the elastic constants criterion. For a cubic crystal, there are three independent elastic constants C_{11}, C_{12} and C_{44}. The mechanical stability can be judged by $C_{11} > 0$, $C_{44} > 0$, $C_{11} > |C_{12}|$ and $(C_{11} + 2C_{12}) > 0$. Fig. 3(a) shows the calculated pressure dependence of elastic constants by a step by step stress–strain method[42,52] for cubic $Fm\bar{3}m$ Ca_2Si. It is obviously that the elastic constants satisfy all the stability conditions shown above, indicating that cubic $Fm\bar{3}m$ Ca_2Si is mechanical stable in the pressure range from −2 to 8 GPa. The positive correlation between the elastic constants and external pressure can be found, which is due to the enhanced interaction between atoms under external pressure.[53] Fig. 3(b) shows the calculated bulk modulus B, Young's modulus E, and shear modulus G from the elastic constants as a function of pressure. As we can see, with the increase of pressure, the mechanical properties of B, E, G increase gradually, which are similar to the trend of elastic constants. Moreover, according to the calculated Poisson's ratio presented in Fig. 3(c), we found that the Poisson's ratio is very small, although it is increasing with the growth of pressure, indicating cubic $Fm\bar{3}m$ Ca_2Si is relatively stable against the shear strain.[54]

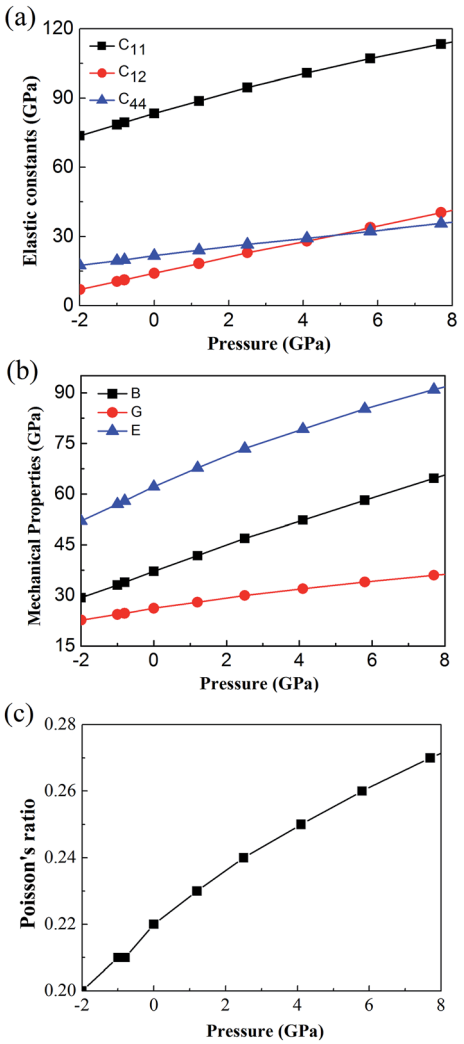

Fig. 3 Calculated (a) elastic constants (b) bulk modulus B, Young's modulus E, shear modulus G and (c) Poisson's ratio of cubic $Fm\bar{3}m$ Ca_2Si as a function of pressure.

In order to get better understanding, we introduced both the standard GGA-PBE functional as well as the HSE06 hybrid functional to calculate the electronic structures. Fig. 4(a) illustrates the total density of states (DOS) for cubic $Fm\bar{3}m$ Ca_2Si. As we can see from the figure, we have obtained 0.59 eV band gap using GGA-PBE functional, agrees well with the previous FPLAPW values of 0.56 eV.[25] It is noted that HSE06 functional enlarges the bandgap to 1.13 eV. The band gap value is obviously larger than the narrow gap Bi_2Te_3-based alloys, which is beneficial for the high temperature thermoelectric applications due to the decrease of the high temperature bipolar conduction

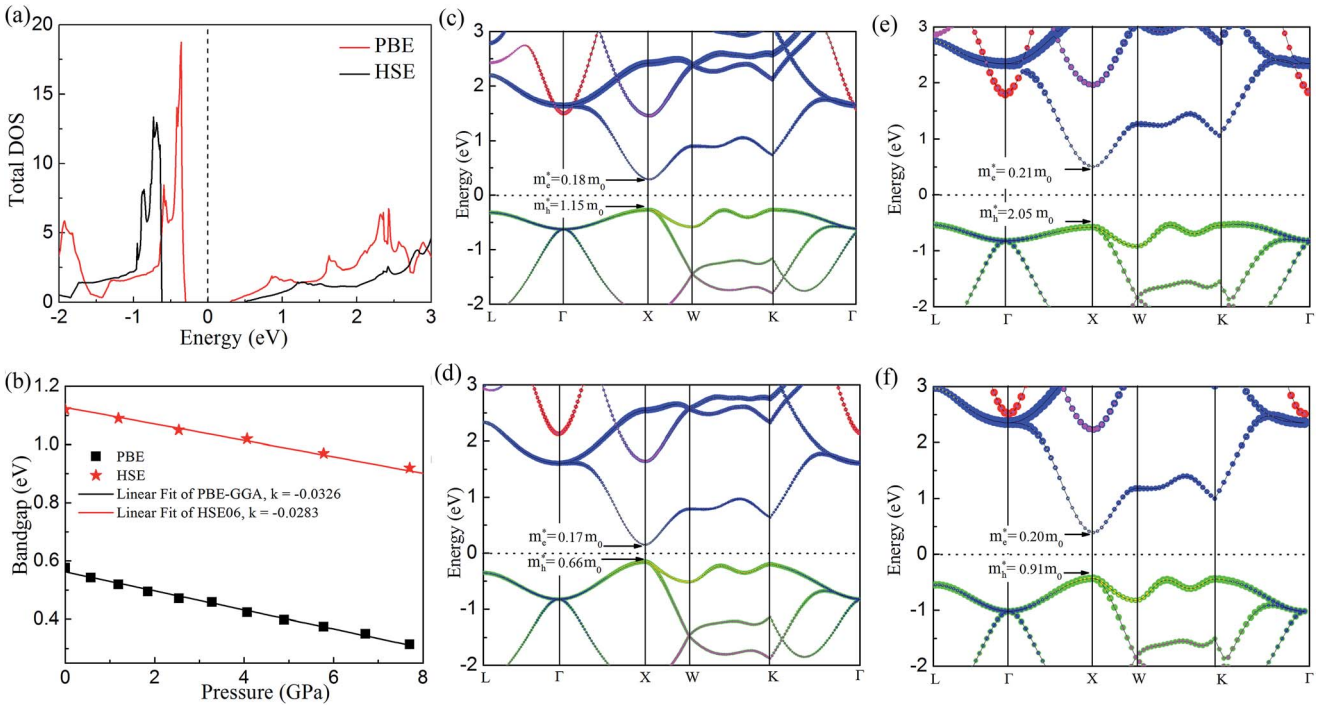

Fig. 4 (a) The total density of states (TDOS) of cubic $Fm\bar{3}m$ Ca_2Si at the ambient condition using PBE and HSE06 functionals. (b) The calculated band gap of cubic $Fm\bar{3}m$ Ca_2Si as a function of pressure. The projected PBE band structure (c) at the ambient condition and (d) at 7.8 GPa external pressure of cubic $Fm\bar{3}m$ Ca_2Si. The projected HSE06 band structure (e) at the ambient condition and (f) at 7.8 GPa external pressure of cubic $Fm\bar{3}m$ Ca_2Si. The Fermi energy is set to 0 eV. The size of red, blue, pink and green circles illustrates the project weight of Ca-s, Ca-d and Si-s Si-p electrons, respectively.

effect.[55] By the analysis of the bandgap at various conditions in Fig. 4(b), we found that both GGA-PBE and HSE06 bandgaps reduce linearly with the increase of the pressure. The fitting slope for the GGA-PBE and HSE06 results are -0.0326 and -0.0283 eV GPa^{-1}, respectively. We have found that GGA-PBE and HSE06 methods present very similar band gap changing tendency of cubic $Fm\bar{3}m$ Ca_2Si under pressure, where the HSE06 gaps are about 0.6 eV larger than the PBE gaps. According to the projected band structure at the ambient condition in Fig. 4(c) and (e), we found that cubic $Fm\bar{3}m$ Ca_2Si has been theoretically predicted to be a direct band gap semiconductor using PBE, where both the valance band maximum (VBM) conduction band minimum (CBM) are located at the X (0.5, 0, 0.5) point of 1BZ. However, for the HSE06 hybrid functional calculation, we found that the energy level of VBM at the L (0.5, 0.5, 0.5) point is slightly ($\sim$0.04 eV) higher than that at the X point. Similar to black phosphorene,[56] we can still briefly consider cubic $Fm\bar{3}m$ Ca_2Si as a direct gap semiconductor using HSE06 as well. For the both cases, the double generated VBM at the X point is mainly occupied by the Si p electrons and the CBM is characterized as the Ca-d electrons. It is worth noting that the Si-p valence band states at the K point and in the middle of the W–K high symmetry tie line show very close energy level to the VBM, agrees well with the previous FPLAPW prediction.[25] These energy states give rise to the flat valence band states and high DOS peaks below the Fermi level and indicate good thermoelectric properties of cubic $Fm\bar{3}m$ Ca_2Si. To verify our hypothesis, we calculated the effective masses of the hole and electron at the X point by fitting the states around the VBM and CBM, respectively. The effective masses of the electron along the X–Γ direction using PBE $m^*_{e,PBE} = 0.18m_e$ and using HSE06 $m^*_{e,HSE06} = 0.21m_e$. The effective masses of the hole along the X–Γ direction using PBE $m^*_{h,PBE} = 1.15m_e$ and using HSE06 $m^*_{h,HSE06} = 2.05m_e$. The outstanding effective masses of the hole indicating the potential high thermoelectric properties with p type doping of cubic $Fm\bar{3}m$ Ca_2Si. According to the projected band structure under 7.8 GPa external pressure in Fig. 4(d) and (f), we found that the effects of the external pressure pull up the energy level of VBM and push down the energy level of CBM at the X point for both PBE and HSE06. As a result, the X to X direct gap nature of cubic $Fm\bar{3}m$ Ca_2Si can be protected. The Ca-s dominated conduction band state at the Γ point and the Si-s dominated conduction band state at the L point move upwards to higher energy levels under certain pressure. Besides, the other valence and conduction states are not sensitive to the external pressure. Herein, the stability of the electronic structure can protect the structure stability of cubic $Fm\bar{3}m$ Ca_2Si. Although the effective masses of the electron are insensitive to the external, however, with the increasing of the pressure up to 7.8 GPa, the effective masses of the hole along the X–Γ direction reduce to $m^*_{h,PBE} = 0.66m_e$ and $m^*_{h,HSE06} = 0.91m_e$. The decreasing of the hole effective mass indicating the increasing of the external pressure cannot improve the thermoelectric properties of cubic $Fm\bar{3}m$ Ca_2Si. Hence combining with the lattice dynamic analysis, our further thermoelectric property study is focused on cubic $Fm\bar{3}m$ Ca_2Si at the ambient conduction.

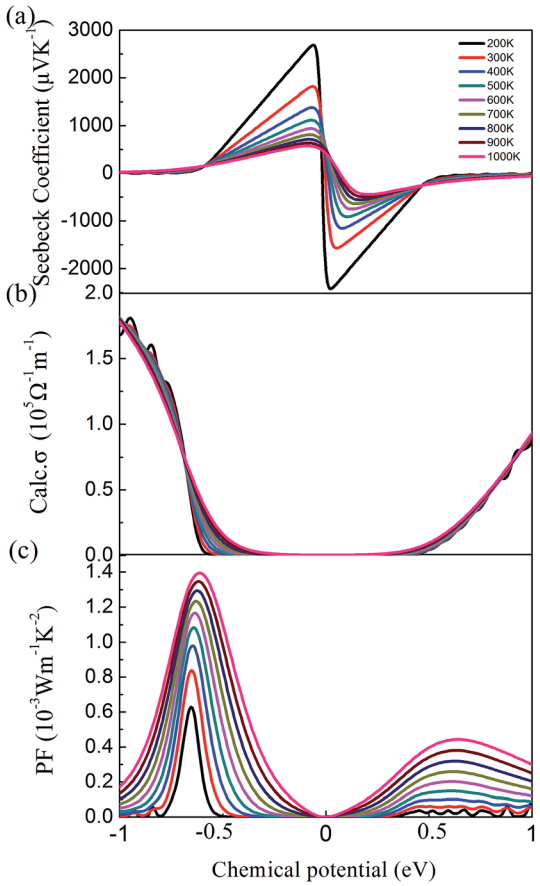

Fig. 5 (a) Calculated Seebeck coefficient, (b) electrical conductivity and (c) power factor of cubic $Fm\bar{3}m$ Ca_2Si as a function of chemical potential.

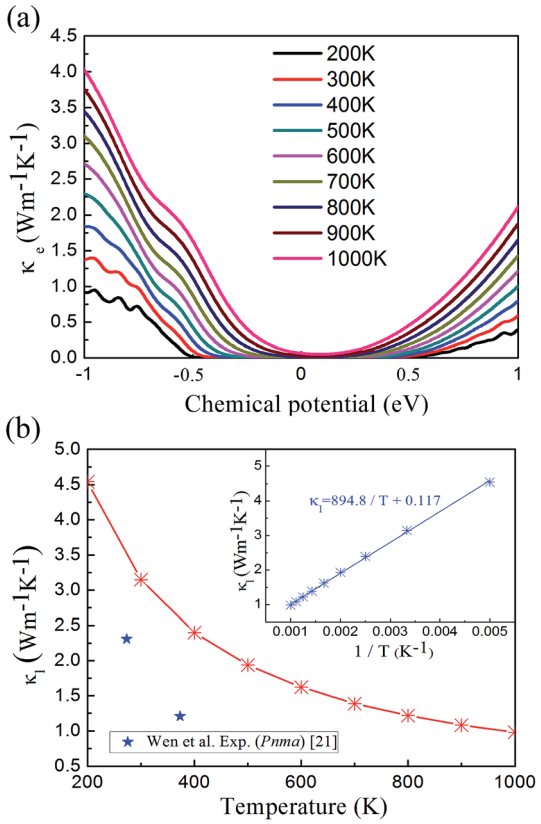

Fig. 6 (a) The electronic thermal conductivity and (b) lattice thermal conductivity of cubic $Fm\bar{3}m$ Ca_2Si as a function of temperature. The star flags are experimental lattice thermal conductivity of *Pnma* Ca_2Si in ref. 21.

By solving the Boltzmann transport equation based on the HSE06 electronic eigenvalues, we first analyzed the thermoelectric power factor (PF) $S^2\sigma$ to examine the thermoelectric properties of cubic $Fm\bar{3}m$ Ca_2Si. The Seebeck coefficients S as a functional of the chemical potential at difference temperature are illustrated in Fig. 5(a). We found that the Seebeck coefficient is very sensitive to the chemical potential. Hence the efficient thermoelectric properties can be tuned *via* the carrier concentration. Generally, we found that the Seebeck coefficient of cubic $Fm\bar{3}m$ Ca_2Si decreases with the increase of temperature. Nevertheless, it is higher than the experimental measured peak value 300 μV K^{-1} for the p-type doped orthorhombic Ca_2Si in most of the chemical potential and temperature range, which indicates that cubic $Fm\bar{3}m$ Ca_2Si is expected to show better thermoelectric performances than the orthorhombic phase. The calculated electrical conductivity σ within the constant relaxation time approximation is plotted in Fig. 5(b). It is easily to understand that there shows a positive correlation between the electrical conductivity and chemical potential, since more positive (negative) chemical potential corresponds to the higher electron (hole) concentration. Hence large chemical potential is expected to achieve high electrical conductivity. However, the thermoelectric PF $S^2\sigma$ does not follow this rule due to the fact that the Seebeck coefficient peaks at chemical potential very close to 0, indicating the finite carrier concentration is needed for the optimized thermoelectric PF. As seen from the calculated thermoelectric PF in Fig. 5(c), the thermoelectric PF reaches a peak around −0.5 to −0.6 eV for the p-type doping and 0.4–0.6 eV for the n-type doping at different temperatures. We found that the thermoelectric PF increases with the increase of temperature, which is contrary to the Seebeck coefficient. It is because the electrical conductivity is gradually increased when the temperature is increasing at the chemical potential larger than −0.64 eV. Moreover, we found that the p-type doping is preferred for the thermoelectric applications of cubic $Fm\bar{3}m$ Ca_2Si with larger optimized thermoelectric PF $S^2\sigma$.

In the denominator of the figure of merit ZT, the thermal conductivity can be divided to the electronic (κ_e) and lattice (κ_l) contribution terms. The electronic thermal conductivity in Fig. 6(a) can also be solved from the well-known Wiedemann–Franz law $\kappa_e = \frac{\pi}{3}\left(\frac{k_B}{e}\right)\sigma T$. Hence as a function of the chemical potential, the electronic thermal conductivity curves present very similar trend to the electrical conductivity. Meanwhile, in the whole chemical potential range, positive correlation can be found between the electronic thermal conductivity and temperature. The lattice thermal conductivity in Fig. 6(b) is estimated by the phonon Boltzmann transport equation. We found that the lattice thermal conductivity of cubic $Fm\bar{3}m$ Ca_2Si

show the same order of magnitude to the *Pnma* Ca_2Si and Bi_2Te_3-based chalcogenides around serval W m^{-1} K^{-1}, which is lower than Mg_2Si as we have anticipated. Considering the large differences between the covalent radii of Ca (1.76 Å) and Si (1.11 Å)[57] as well as the soft mode nature of the phonon dispersion curves, the low lattice thermal conductivities can be understood. As seen in the insert figure of Fig. 6(b), the lattice thermal conductivity can be linearly fitted to the reciprocal of temperature, indicating the fact that the phonon scattering is dominated by the anharmonic phonon–phonon interactions. To the better understanding of the low thermal conductivity, we analyze the Grüneisen parameter to quantify the anharmonicity. The average Grüneisen parameter is 1.97 for cubic $Fm\bar{3}m$ Ca_2Si, which is comparable with typical thermoelectric materials PbTe of 1.96 with low thermal conductivity.[58]

After all, we can evaluate the thermoelectric figure of merit *ZT* based on the above results. Fig. 7(a) illustrates the calculated *ZT* as a function of the chemical potential. We found that the plot of *ZT* shows very similar feature to the plot of PF, and it is interesting that *ZT* increases with the increase of temperature up to 1000 K. The peak values of *ZT* at different temperatures are plotted in Fig. 7(b). The maximal *ZT* value of 0.07 and 0.52 are observed with the chemical potential of −0.628 eV and −0.533 eV at 300 K and 1000 K, corresponding to the hole concentration of 2.45×10^{18} cm^{-3} and 2.83×10^{18} cm^{-3}, respectively. The *ZT* value of the p-type doped *Pnma* Ca_2Si is 2×10^{-5} around 350 K (ref. 21) (marked as the violet star in Fig. 7(b)), which is much smaller than our predicted values for the cubic $Fm\bar{3}m$ Ca_2Si. As seen the *ZT* of intrinsic Mg_2Si in Fig. 7(b), we found that the thermoelectric properties of cubic $Fm\bar{3}m$ Ca_2Si are comparable to intrinsic Mg_2Si.[59,60] Since the solid solution treatment and doping can effectively enhance the figure of merit *ZT* of Mg_2Si to as large as 1.1 (ref. 61), further optimizing of the thermoelectric properties of the cubic $Fm\bar{3}m$ Ca_2Si is anticipated.

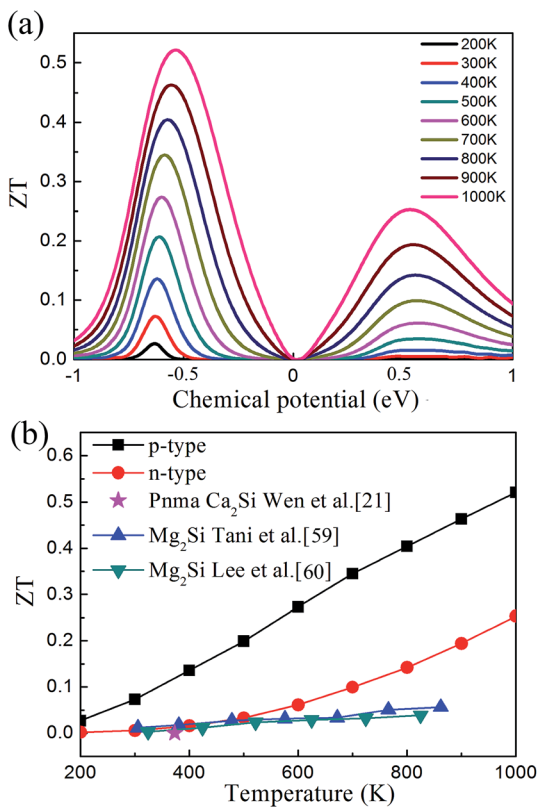

Fig. 7 (a) Thermoelectric figure of merit *ZT* of cubic $Fm\bar{3}m$ Ca_2Si as a function of chemical potential. (b) The maximum *ZT* of cubic $Fm\bar{3}m$ Ca_2Si as a function of temperature.

4. Conclusion

In summary, based on the *ab initio* evolutionary algorithm structure searching and density functional theory calculations, we have found that the orthorhombic *Pnma* phase is the most stable structure at pressure higher than −0.82 GPa, while the cubic $Fm\bar{3}m$ phase is a meta-stable one in certain conditions. The stability of the cubic $Fm\bar{3}m$ Ca_2Si has been confirmed by the lattice dynamical phonon dispersion calculations and the mechanic criterion studies. The direct bandgap nature of cubic $Fm\bar{3}m$ Ca_2Si at various conditions was explored. Combining the HSE06 hybrid functional calculations, Boltzmann transport equation and the phonon Boltzmann transport equation, we have theoretically predicted the thermoelectric properties of cubic $Fm\bar{3}m$ Ca_2Si, which present larger Seebeck coefficient than orthorhombic Ca_2Si. The optimized thermoelectric figure of merit *ZT* value of 0.52 is achieved for the p-type doping with the hole concentration 2.83×10^{18} cm^{-3} at 1000 K. We expect our findings will facilitate the experimental synthesis of Ca_2Si isomers as well as their practical applications in thermoelectric devices.

Acknowledgements

This work was financially supported by the National Natural Science Foundation of China (No. 61504028, 61274005, 51301039, 11347007 and 11674131), the National Natural Science Foundation for Distinguished Young Scientists of China (Grant No. 51225205), the Natural Science Foundation of Fujian Province (No. 2016J01214 and 2016J01216), the Qing Lan Project, and the Priority Academic Program Development of Jiangsu Higher Education Institutions (PAPD).

References

1 M. Beekman, D. T. Morelli and G. S. Nolas, *Nat. Mater.*, 2015, **14**, 1182–1185.
2 J. Yang, L. Xi, W. Qiu, L. Wu, X. Shi, L. Chen, J. Yang, W. Zhang, C. Uher and D. J. Singh, *npj Computational Materials*, 2016, **2**, 15015.
3 J. Zhou, B. Sa and Z. Sun, *Intermetallics*, 2010, **18**, 2394–2398.
4 J. Zhou, Z. Sun, X. Cheng and Y. Zhang, *Intermetallics*, 2009, **17**, 995–999.
5 N. Miao, J. Zhou, B. Sa, B. Xu and Z. Sun, *Appl. Phys. Lett.*, 2016, **108**, 213902.
6 H. Zhu, W. Sun, R. Armiento, P. Lazic and G. Ceder, *Appl. Phys. Lett.*, 2014, **104**, 082107.

7 I. Gonzalez-Valls and M. Lira-Cantu, *Energy Environ. Sci.*, 2009, **2**, 19–34.
8 D. Parker, X. Chen and D. J. Singh, *Phys. Rev. Lett.*, 2013, **110**, 146601.
9 D. I. Bilc, G. Hautier, D. Waroquiers, G. M. Rignanese and P. Ghosez, *Phys. Rev. Lett.*, 2015, **114**, 136601.
10 S. Xun and L. Chen, *Nat. Mater.*, 2016, **15**, 691–692.
11 B. Poudel, Q. Hao, Y. Ma, Y. Lan, A. Minnich, B. Yu, X. Yan, D. Wang, A. Muto, D. Vashaee, X. Chen, J. Liu, M. S. Dresselhaus, G. Chen and Z. Ren, *Science*, 2008, **320**, 634–638.
12 R. Venkatasubramanian, E. Siivola, T. Colpitts and B. O'Quinn, *Nature*, 2001, **413**, 597–602.
13 F. Q. Wang, S. Zhang, J. Yu and Q. Wang, *Nanoscale*, 2015, **7**, 15962–15970.
14 H. Zhao, J. Sui, Z. Tang, Y. Lan, Q. Jie, D. Kraemer, K. Mcenaney, A. Guloy, G. Chen and Z. Ren, *Nano Energy*, 2014, **7**, 97–103.
15 N. Miao and P. Ghosez, *J. Phys. Chem. C*, 2015, **119**, 14017–14022.
16 P. Ying, X. Liu, C. Fu, X. Yue, H. Xie, X. Zhao, W. Zhang and T. Zhu, *Chem. Mater.*, 2015, **27**, 909–913.
17 T. D. Huan, V. N. Tuoc, N. B. Le, N. V. Minh and L. M. Woods, *Phys. Rev. B: Condens. Matter Mater. Phys.*, 2016, **93**, 094109.
18 C. Wen, T. Nonomura, Y. Warashina, Y. Kubota, T. Nakamura, Y. Hayakawa, M. Tanaka, K. Isobe and H. Tatsuoka, *Int. J. Mater. Res.*, 2011, **102**, 401–405.
19 C. Wen, A. Kato, T. Nonomura and H. Tatsuoka, *J. Alloys Compd.*, 2011, **509**, 4583–4587.
20 C. Wen, T. Nonomura, K. Isobe, Y. Kubota, T. Nakamura, Y. Hayakawa, A. Kato and H. Tatsuoka, *IOP Conf. Ser.: Mater. Sci. Eng.*, 2011, **18**, 142014.
21 C. Wen, T. Nonomura, A. Kato, Y. Kenichi, H. Udono, K. Isobe, M. Otake, Y. Kubota, T. Nakamura, Y. Hayakawa and H. Tatsuoka, *Phys. Procedia*, 2011, **11**, 106–109.
22 P. Eckerlin, E. Leicht and E. Wölfel, *Z. Anorg. Allg. Chem.*, 1961, **307**, 145–156.
23 Z. Yang, D. Shi, B. Wen, R. Melnik, S. Yao and T. Li, *J. Solid State Chem.*, 2010, **183**, 136–143.
24 J.-I. Tani and H. Kido, *Comput. Mater. Sci.*, 2015, **97**, 36–41.
25 D. B. Migas, L. Miglio, V. L. Shaposhnikov and V. E. Borisenko, *Phys. Rev. B: Condens. Matter Mater. Phys.*, 2003, **67**, 205203.
26 S. Lebègue, B. Arnaud and M. Alouani, *Phys. Rev. B: Condens. Matter Mater. Phys.*, 2005, **72**, 085103.
27 T. Sakamoto, T. Iida, A. Matsumoto, Y. Honda, T. Nemoto, J. Sato, T. Nakajima, H. Taguchi and Y. Takanashi, *J. Electron. Mater.*, 2010, **39**, 1708–1713.
28 J. D. Boor, C. Compere, T. Dasgupta, C. Stiewe, H. Kolb, A. Schmitz and E. Mueller, *J. Mater. Sci.*, 2014, **49**, 3196–3204.
29 Y. L. Li, W. Luo, Z. Zeng, H. Q. Lin, H. K. Mao and R. Ahuja, *Proc. Natl. Acad. Sci. U. S. A.*, 2013, **110**, 9289–9294.
30 B. Sa, J. Zhou, Z. Song, Z. Sun and R. Ahuja, *Phys. Rev. B: Condens. Matter Mater. Phys.*, 2011, **84**, 085130.
31 Z. Sun, J. Zhou, Y. Pan, Z. Song, H. K. Mao and R. Ahuja, *Proc. Natl. Acad. Sci. U. S. A.*, 2011, **108**, 10410–10414.
32 J. Hafner, *J. Comput. Chem.*, 2008, **29**, 2044–2078.
33 J. P. Perdew and Y. Wang, *Phys. Rev. B: Condens. Matter*, 1992, **45**, 13244.
34 J. P. Perdew, K. Burke and M. Ernzerhof, *Phys. Rev. Lett.*, 1996, **77**, 3865.
35 C. W. Glass, A. R. Oganov and N. Hansen, *Comput. Phys. Commun.*, 2006, **175**, 713–720.
36 A. R. Oganov and C. W. Glass, *J. Chem. Phys.*, 2006, **124**, 244704.
37 Y. Wang, L.-Q. Chen and Z.-K. Liu, *Comput. Phys. Commun.*, 2014, **185**, 2950–2968.
38 S. Baroni, S. De Gironcoli, A. Dal Corso and P. Giannozzi, *Rev. Mod. Phys.*, 2001, **73**, 515–562.
39 M. B. Taylor, G. D. Barrera, N. L. Allan and T. H. K. Barron, *Phys. Rev. B: Condens. Matter Mater. Phys.*, 1997, **56**, 14380.
40 K. Momma and F. Izumi, *J. Appl. Crystallogr.*, 2011, **44**, 1272–1276.
41 J. Muscat, A. Wander and N. M. Harrison, *Chem. Phys. Lett.*, 2001, **342**, 397–401.
42 B. Sa, J. Zhou, R. Ahuja and Z. Sun, *Comput. Mater. Sci.*, 2014, **82**, 66–69.
43 J. Paier, M. Marsman, K. Hummer, G. Kresse, I. C. Gerber and J. G. Angyán, *J. Chem. Phys.*, 2006, **124**, 154709.
44 N. Miao, B. Xu, N. C. Bristowe, D. I. Bilc, M. J. Verstraete and P. Ghosez, *J. Phys. Chem. C*, 2016, **120**, 9112–9121.
45 G. K. H. Madsen and D. J. Singh, *Comput. Phys. Commun.*, 2006, **175**, 67–71.
46 A. Togo, F. Oba and I. Tanaka, *Phys. Rev. B: Condens. Matter Mater. Phys.*, 2008, **78**, 134106.
47 W. Li, J. Carrete, N. A. Katcho and N. Mingo, *Comput. Phys. Commun.*, 2014, **185**, 1747–1758.
48 P. Manfrinetti and A. Palenzona, *Intermetallics*, 2000, **8**, 223–228.
49 A. Khare, B. Himmetoglu, M. Johnson, D. J. Norris, M. Cococcioni and E. S. Aydil, *Appl. Phys. Lett.*, 2012, **111**, 083707.
50 W. Schweika, R. P. Hermann, M. Prager, J. Persson and V. Keppens, *Phys. Rev. Lett.*, 2007, **99**, 125501.
51 W. Li, L. Lindsay, D. A. Broido, D. A. Stewart and N. Mingo, *Phys. Rev. B: Condens. Matter Mater. Phys.*, 2012, **86**, 174307.
52 Z. Sun, R. Ahuja and J. E. Lowther, *Solid State Commun.*, 2010, **150**, 697–700.
53 B. Sa, J. Zhou and Z. Sun, *Intermetallics*, 2012, **22**, 92–98.
54 N. Miao, B. Sa, J. Zhou and Z. Sun, *Comput. Mater. Sci.*, 2010, **50**, 1559–1566.
55 H. Shi, D. Parker, M. H. Du and D. J. Singh, *Phys. Rev. Appl.*, 2015, **3**, 014004.
56 B. Sa, Y. L. Li, J. Qi, R. Ahuja and Z. Sun, *J. Phys. Chem. C*, 2014, **118**, 26560–26568.
57 B. Cordero, V. Gómez, A. E. Platero-Prats, M. Revés, J. Echeverría, C. E. F. Barragán and S. Alvarez, *Dalton Trans.*, 2008, **21**, 2832–2838.
58 Y. Zhang, X. Ke, C. Chen, J. Yang and P. Kent, *Phys. Rev. B: Condens. Matter Mater. Phys.*, 2009, **80**, 024304.
59 J.-I. Tani and H. Kido, *Intermetallics*, 2007, **15**, 1202–1207.
60 H. J. Lee, Y. R. Cho and I.-H. Kim, *J. Ceram. Process. Res.*, 2011, **12**, 16–20.
61 G. Jiang, J. He, T. Zhu, C. Fu, X. Liu, L. Hu and X. Zhao, *Adv. Funct. Mater.*, 2014, **24**, 3776–3781.